High temperature magnetic and structural transformations in Fe-Pd nanowires

Paula G. Bercoff[1,2*], Eva Céspedes[3], Soledad Aprea[1,2] Silvia E. Urreta[1], José Luis Martínez[3], Manuel Vázquez[3]

[1] Universidad Nacional de Córdoba. Facultad de Matemática, Astronomía, Física y Computación. Ciudad Universitaria, 5000 Córdoba, Argentina.
[2] CONICET, Instituto de Física Enrique Gaviola (IFEG). Ciudad Universitaria, 5000 Córdoba, Argentina.
[3] Instituto de Ciencia de Materiales de Madrid, CSIC. E-28049 Madrid, Spain

Corresponding author: Paula G. Bercoff.
bercoff@famaf.unc.edu.ar; paula.bercoff@unc.edu.ar
Tel: +54 351 53 53 701 (ext. 41103)

Abstract
The microstructure and the hysteresis properties of Fe-Pd nanowire arrays were studied in the as-electrodeposited condition at 300 K, and as functions of temperature after a thermal cycle between 300 K and 950 K. $Fe_{36}Pd_{64}$ and $Fe_{65}Pd_{35}$ nanowires, 200 nm in diameter and 7-10 µm long, were electrodeposited into commercial 26 % porosity alumina templates. Initially, the main magnetic phase in both arrays is the metastable γ-Pd(Fe) disordered phase. After a thermal cycle up to 950 K the microstructures transform into a majority ferromagnetic ordered phase ($FePd_3$ in $Fe_{36}Pd_{64}$ and Fe_3Pd in $Fe_{65}Pd_{35}$) embedding γ-Pd(Fe) remaining grains. Curie temperatures result 500 K, 550 K and 900 K for Fe_3Pd, $FePd_3$ and γ-Pd(Fe), respectively. The temperature dependence of the magnetic properties exhibits two stages: one below 500-550 K, when the two phases are ferromagnetic and another one above this temperature when only the minority γ-Pd(Fe) is ferromagnetic. Coercivity and remanence exhibit a maximum near the Curie temperature of the corresponding ordered phase. The effective magnetic anisotropy K_{eff} remains high up to the magnetic transition (ferro to paramagnetic) of the ordered phase, due to the contribution of the magnetocrystalline anisotropy of these relatively hard phases. At higher temperature, the effective anisotropy mainly arises from the magnetostatic (shape and inter-wire dipolar interactions) contribution of the minority phase. The polarization reversal mechanism in the γ-Pd(Fe) phase is found to be the nucleation of inverse magnetic domains and the further expansion of the domain walls into the ferromagnetic grains, surrounded by the paramagnetic ordered phase.

Keywords: Fe-Pd nanowires; Biphase magnetic systems; Metastable phases; Magnetic properties; Magnetization process.

1. Introduction

Nanowires consisting of a noble and a magnetic metal have proven to be quite useful in many fields such as sensing, catalysis, optical detection, and biomedical applications [1]. These bimetallic nanostructures with high aspect ratios like nanowires (NWs) and nanotubes (NTs) can be successfully obtained by low-cost electrochemical techniques, with the advantage of being easily scalable to the industrial production. The particular microstructures and the magnetic hysteresis properties resulting from different template geometries and alloy compositions, in both the as-deposited condition and after high temperature heat treatments, have been widely investigated at room and lower temperature regimes. Examples are Fe-Pt and Co-Pt [2], Fe-Co [3,4], Co-Pd [5,6], Fe-Rh [7] and Fe-Pd [8-11] systems. On the contrary, phase selection,

microstructure and the magnetic hysteresis properties at temperatures well above room temperature are less known. In fact, the phase diagram of these binary alloys is very rich and diverse in the high temperature range, which anticipates a large variety of magnetic phenomena. All the main phases in the binary Fe-Pd system are found to exhibit specific properties. For example, the value of linear magnetostriction, λ, in Fe_xPd_{100-x} alloys depends sensitively on the heat treatment conditions. In the cooled state from 900°C, the concentration dependence of λ at room temperature displays a pronounced maximum at 33 at. % Pd, of about 85×10^{-6} at 500 Oe [12]. In the composition range $60 \leq x \leq 70$, the spontaneous volume magnetostriction scales linearly with the square of magnetization [13].

On the other hand, alloys of composition close to Fe_3Pd have high saturation magnetization, approximately 2/3 of that of Fe at room temperature, and undergo a highly reversible face-centered cubic (*fcc*) to face-centered tetragonal (*fct*) transformation, being very promising candidates for applications as ferromagnetic shape memory alloys [14, 15], or to enhance SERS-active substrates [16].

The **martensitic** transformation (**MT**) starting, M_s, and finishing M_f, temperatures in bulk samples were found to be $M_s = 40$ °C and $M_f = 12$ °C **[17].**

Disordered metastable Fe_xPd_{100-x} alloys with $60 \leq x \leq 70$, evidence a quite small value of the thermal expansion coefficient near 100 °C (Invar property) [18,19]. Particularly, the alloy with x = 68.8 shows a giant magnetostriction of $\cong 3$ %, at 77 K [20].

Soft ferromagnetic $FePd_3$ ordered alloys also exhibit an anomalously low thermal expansion at high applied pressures [21-23]. In addition, the $FePd_3$ alloy can be used in electrocatalysis to enhance the cycle stability of hybrid Li–air batteries [24] or as an electrocatalyst in different reactions [10, 25-29]. These magnetic catalysts can also be easily recovered for reuse.

All the mentioned phases are ferromagnetic at and below room temperature. Then, depending on whether the constitutive phases are stable and/or metastable, which are their volume fractions, sizes and distributions, and also on the proximity to the Curie temperature of each one, different hysteresis properties are expected above room temperature.

In a recent paper, we have reported interesting results on the magnetic anisotropy temperature dependence of $Fe_{65}Pd_{35}$ NWs below room temperature [9]. Unlike the NWs of the present paper, those were synthesized at room temperature and only disordered cubic phases were obtained, with no traces of an ordered phase. In this work, we investigate the structural phases and the hysteresis properties of Fe-Pd NWs of two different compositions: one in the region of stability of the $FePd_3$ ordered phase at low temperature ($Fe_{36}Pd_{64}$) and the other one in the region of coexistence of the ordered FePd and the α-Fe(Pd) phases below 600 °C ($Fe_{65}Pd_{35}$). Performing the electrochemical synthesis at a slightly higher temperature (40 °C instead of room temperature) allows the formation of metastable phases which have not been reported before for this kind of NWs, providing a strong motivation for studying their magnetic properties in a wide range of temperatures.

All the NW arrays were first studied in the as-deposited state. Then, the stationary final phase selection after thermal cycling up to 950 K was determined, and the magnetic properties of these final microstructures were measured in the temperature range between 300 K and 950 K. The aim is to explore magnetic transitions at high temperature in these low dimensional nanostructures as well as to investigate in more detail the magnetic behavior of less-common Fe-Pd metastable phases at high temperature.

2. Experimental procedures

Fe-Pd nanowires were electro-synthesized using alumina porous membranes (AAO, provided by Whatman Co.) as templates, and electrolytic baths with $FeCl_3$ and $PdCl_2$ salts in ultrapure water. The supporting electrolyte was ammonium citrate 0.3 M, with ammonium hydroxide 0.25 M added to the solution to keep the pH = 9.00. The NWs composition was controlled by changing the Fe^{3+} and Pd^{2+} ions concentration in the electrolytic bath. Fe36 and Fe65 NWs were obtained using ion ratios of $[Fe^{3+}]/[Pd^{2+}] = 25/30$ and 50/20 mM, respectively.

The commercial AAO membranes were 60 μm-thick, with nominal pore size diameter $D = 200$ nm and a pore center-to-center distance $d_{cc} = 370$ nm, rendering a porosity P = 26%, with $P = \pi/2\sqrt{3}(D/d_{cc})^2$. Prior to use, a conductive thin gold layer was sputtered on one side of the membranes (open by both sides), to be used as cathode. Electrodeposition was carried out at 40ºC in order to promote crystallization of the desired phases, using a potentiostat/galvanostat Autolab and a three-electrode cell: a commercial Ag/AgCl electrode was used as reference and a Pt wire as a counter electrode. The electrodeposition potential was −1.5 V *vs.* Ag/AgCl, during a deposition time of 30 min.

The samples' morphology was studied using a Sigma Zeiss Field Emission Scanning Electron Microscope (FE-SEM), with an attached Oxford Energy Dispersive Spectrometer (EDS) which allowed determining the chemical composition. SEM images were taken after dissolving the AAO template in order to release the NWs. The mean composition of the samples was determined by EDS after measuring many relatively large zones in each sample to improve the statistical error, which in all cases was ±2 at. %.

The total volume of metallic NWs in the array was roughly estimated by considering each template's porosity, and the mean geometric parameters of each kind of NW, as determined by SEM images.

Phase characterization was carried out using X-ray diffraction (XRD) on two diffractometers: a Bruker D8 Advance and a PANalytical PW3830, using Cu Kα radiation (λ = 0.15418 nm) in the Bragg-Brentano configuration.

Magnetic properties were measured with a SQUID magnetometer (MPMS-3), from Quantum Design (San Diego, USA), allowing an applied magnetic field up to 7 T. The furnace option, which allows sensitive magnetometry measurements at controlled high temperatures, was used to measure between 300 K and 950 K. Heating is achieved by a resistive heating element, which is lithographically patterned onto the custom-designed sample holder. A thermocouple embedded at the holder back side measures the temperature in the sample region, and a thermistor at the top connector corrects for heating of the cold junction. To maximize thermal contact, samples were

attached to the heater stick using an alumina-based cement. To reduce thermal gradients, the platinum heater zone was wrapped with a thin copper-foil for radiation shield. A turbo pump was used for vacuum generation in the sample chamber to avoid helium boiling-off. Thermal cycles were performed at a constant rate of 10 K/min between room temperature and 950 K, and hysteresis loops up to 7 T where measured at different temperatures between 300 K and 950 K.

In addition to magnetization measurement during thermal cycling, the evolution of the initial phase microstructure was explored with Differential Thermal Analysis (DTA) and Thermogravimetric Analysis (TGA) techniques, in a TA device, during heating in Ar atmosphere at a rate of 10 K/min.

The samples studied in this work are denoted by their mean iron at. % composition that is, Fex ≡ Fe$_x$Pd$_{100-x}$ (x = 36, 65).

3. Results and discussion

3.1. *Morphology*
SEM images of the NWs after partial dissolution of the alumina templates are displayed in Figure 1 for samples Fe36 (1a) and Fe65 (1b). The NWs replicate the pore cylindrical shape with a quite constant diameter (200 nm); lengths L of 10 μm (Fe36) and 7 μm (Fe65) are obtained, resulting in relatively large aspect ratios in both cases ($A_R = L/D \sim 50$ and 35, respectively).
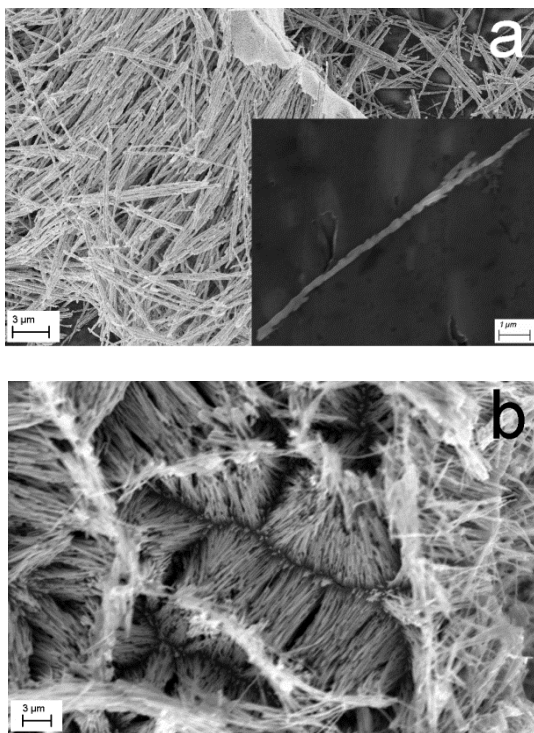

Figure 1. SEM images corresponding to NWs of arrays (a) Fe36 and (b) Fe65, after being partially released from the alumina template.

3.2. *Phases and Crystallography*
The X-ray diffractograms displayed in Figure 2 show the room temperature patterns corresponding to the arrays in the as-deposited condition, measured with the X-ray beam incident on the arrays bottom surface, after removing the gold layer. In Fe36 the main magnetic phase is the γ−Pd(Fe) *fcc* disordered (A1) solid solution. Extra peaks of PdO, related to a minor contribution, are detected, likely arising from oxidation during electrodeposition. On the contrary, as-deposited Fe65 NWs are biphasic, containing −in addition to γ−Pd(Fe) − a small volume fraction of the Fe$_3$Pd *Pm$\bar{3}$m (221)* L1$_2$ ordered phase. Diffraction peaks from Fe$_2$O$_3$ are observed in this case, which correspond to a very small proportion of this phase, likely formed during air/water exposition during the removal of the sputtered gold contact. This contribution, arising from the most reactive top layer on the NWs tip, represents just a minor surface contribution compared to the NWs bulk one.
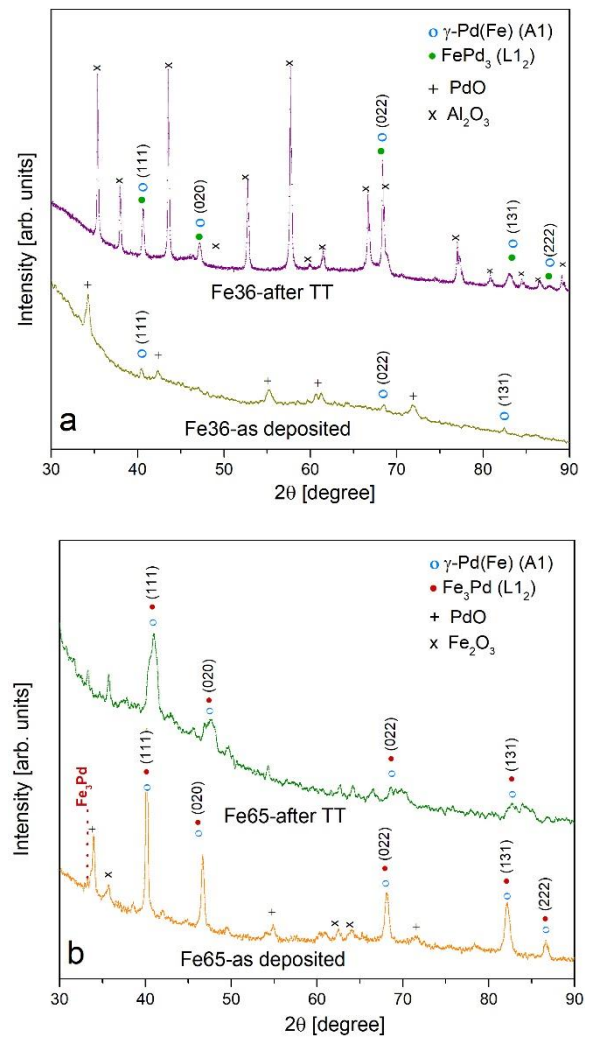

Figure 2. X-ray diffractograms of (a) Fe36 and (b) Fe65 in the as-deposited state and after a heating-cooling thermal cycle (TT), between 300 K and 950 K at 10 K/min.

The equilibrium phase diagram of Fe-Pd alloys [30] indicates that a paramagnetic γ-Fe_xPd_{100-x} (A1) disordered *fcc* solid solution is the stable phase at high temperature, in all the composition range (**see Figure 3**). At lower temperatures and for larger iron contents ($x \geq 70$) an α-Fe_xPd_{100-x} alloy, having a *bcc*-type structure is predicted, and for $x \leq 60$ a *fcc*-type lattice has also been reported [31]. In spite of that, the NWs electrodeposited in this work, with different compositions, all exhibit a metastable *fcc* disordered structure, and contrarily to the high temperature γ-Fe_xPd_{100-x} phase, it is ferromagnetic as will be shown below.

Figure 2 shows the X-ray diffractograms of Fe36 and Fe65 nanowire arrays in the as-deposited state and after a heating-cooling thermal treatment cycle between 300 K and 950 K at 10 K/min.
From the data in Figure 2, crystalline phases were identified, the mean crystallite size, the lattice parameter, and phase volume fractions were estimated for each array in the as-deposited condition, and the results are condensed in Table 2.
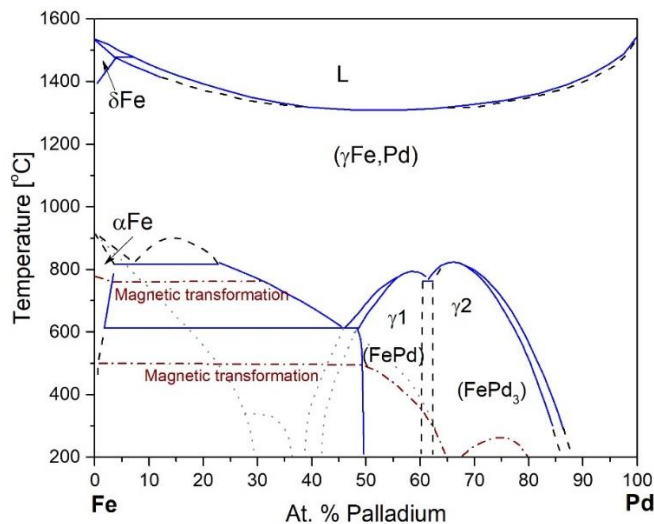

Figure 3. Binary Fe-Pd phase diagram (adapted from [32]). Extensions of metastable phase fields are marked as dotted lines, while magnetic transformations are indicated with dash-dotted lines.

Then, it is concluded that at room temperature, NWs in the as-deposited condition are composed of a metastable *fcc*-type ferromagnetic phase. In Fe65 NWs, a quite small volume of the stoichiometric ordered phase Fe_3Pd is also present, despite it has been reported that this phase is not stable [33]. It is worth noting that this **iron-rich Fe_3Pd phase exhibits** a larger lattice parameter in the as-deposited state as compared to that in the thermal treatment (TT) condition, after a thermal cycle between 300 K and 950 K.

3.3 *Thermal treatment cycling (TT)*
The evolution of the initial γ–Fe(Pd) *fcc* metastable phase at higher temperatures was investigated by performing a heating-cooling thermal cycle between 300 K to 950 K, at a constant rate of 10 K/min. The temperature dependence of the array's magnetic polarization was measured under an external magnetic field of 100 mT, applied parallel (PA orientation) to the NW's long axis. The first heating-cooling cycles corresponding to Fe36 and Fe65 are shown in **Figure 4a and 4b**, respectively. As expected, all the curves show heating-cooling hysteresis arising from the structural transformation of the initial metastable phases into other/s more stable ones. In addition, ordering and magnetic transformations cannot, in principle, be excluded.
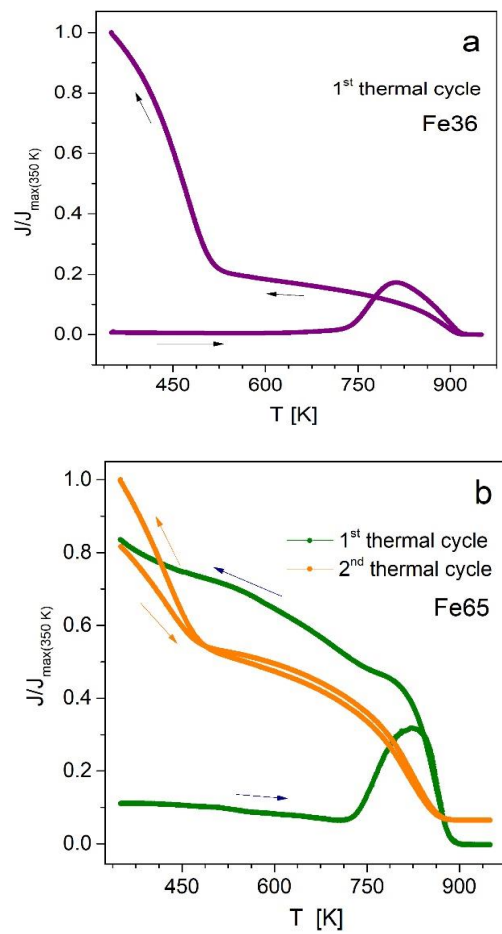

Figure 4. Relative magnetic polarization as a function of temperature during the first heating-cooling cycle after electrodeposition, for arrays (a) Fe36 and (b) Fe65. Measurements are performed under an external magnetic field of 100 mT. The relative polarization *vs.* temperature curve for the second subsequent thermal cycle in the same temperature range in Fe65 is also depicted in (b). Large heating-cooling hysteresis is absent in the second cycle.

In both as-deposited arrays, Fe36 and Fe65, magnetic polarization remains relatively low during heating up to about 700 K, where it increases to reach a local maximum near 820 K to further decrease reaching a

4

constant value above 900 K. During the subsequent cooling, the magnetic polarization in the two arrays monotonously increases as temperature descends, leading to a large hysteresis. This behavior is consistent with the transformation of a given volume of the initial $\gamma-$Fe(Pd) *fcc* solid solution into the FePd$_3$ (Fe36) and Fe$_3$Pd (Fe65), L1$_2$ ordered phases. Once these phases form, no large additional changes in microstructure take place, as observed in **Figure 4b** for sample Fe65, with quite small hysteresis in the second heating-cooling cycle. It is worth noting that during cooling, both polarization *vs.* temperature curves undergo a slope change, being this feature more marked during the second heating-cooling cycle (see **Figure 4b**). This change takes place near 550 K in Fe36 and near 500 K in Fe65, respectively.

The phases obtained after the thermal cycle between 300 K and 950 K were identified with XRD techniques and the resulting diffractograms, depicted in Figure 2,

are compared to those measured in the as-deposited arrays. The main parameters' values are summarized in Table 2.

As depicted in Table 2, Fe36 in the initial state is composed of 100% of A1 γ-Pd(Fe) phase, while after the thermal cycle the L1$_2$ ordered FePd$_3$ phase appears. In Fe65, a small volume fraction of the L1$_2$ ordered Fe$_3$Pd phase is present in the as-deposited array, in agreement with a larger amount of iron in this sample, and after the heat treatment this ordered phase predominates.

At room temperature, all these phases are ferromagnetic [34]; the Curie temperature of the L1$_2$ ordered FePd$_3$ phase is reported to be $T_C = 545$ K [35] and the Curie temperature of the L1$_2$ metastable ordered Fe$_3$Pd phase is about $T_C \approx 570$ K [36], being 30 K lower in the perfectly ordered configuration ($T_C \approx 540$ K).

Table 2. Main phases, their symmetry and volume fractions (*Vol.*), the lattice parameter *a*, and the mean crystallite size d_{SCH}, estimated for each array (Fe*x*) in the as-deposited condition and after a thermal cycle 300K – 950 K – 300 K (Fe*x*-TT) are included.

	Phases	*Vol.* [%]	*Symmetry*	a [Å] [a]	a [Å] [b]	$d_{SCH} \pm 10$ [nm]
Fe36	A1-γ-Pd(Fe) ICSD 103585	100	$Fm\bar{3}m$ (225)	3.8873(4)	3.890(6)	40
Fe36-TT	A1-γ- Pd(Fe) ICSD 103585	24	$Fm\bar{3}m$ (225)	3.8873(4)	3.865(4)	50
	FePd$_3$ ICSD 103582	76	$Pm\bar{3}m$ (221) (L1$_2$)	3.8550(1)	3.866(3)	10
Fe65	A1-γ-Pd(Fe) ICSD 103585	90	$Fm\bar{3}m$ (225)	3.8873(4)	3.891(1)	30
	Fe$_3$Pd ICSD 103586	10	$Pm\bar{3}m$ (221) L1$_2$	3.8180(1)	3.894(7)	30
Fe65-TT	A1-γ-Pd(Fe) ICSD 103585	33	$Fm\bar{3}m$ (225)	3.8873(4)	3.869(1)	20
	Fe$_3$Pd ICSD 103586	67	$Pm\bar{3}m$ (221) L1$_2$	3.8180(1)	3.813(1)	20

a [a] From ICSD database a [b] This work

The magnetic transition temperature for the A1 γ-Fe$_x$Pd$_{100-x}$ solid solution is more complex as the Curie temperature is not a monotonic function of composition but goes through a maximum near $x = 53$, as reported by Burzo et al. [34]. For the disordered A1 γ- Fe$_x$Pd$_{100-x}$ phase, these authors predict a Curie temperature of 550 K and 650 K for nominal compositions corresponding to

Fe36 and Fe65 NWs, respectively. In the present work, the magnetization drop at about 900 K is associated with the ferro-paramagnetic transition of this A1 γ- Fe$_x$Pd$_{100-x}$ phase, while the abrupt slope change at lower temperature near the end of the temperature cycle is assigned to the magnetic transformation of the ordered

stoichiometric phases at the Curie temperature of about $T_C \sim 500$ K.

The evolution of the initial distribution of metastable phases was further investigated by Thermogravimetric Analysis (TGA) and Differential Thermal Analysis (DTA) techniques between room temperature and 1000 K. **Figure 5** shows the results of the thermogravimetric and differential thermal analysis for the investigated arrays. The TGA curve (**Figure 5a**) indicates a progressive water vapor weight loss from room temperature to 700 K– 800 K, depending on the array, which amounted to a total of 7% (Fe36) and 14% (Fe65).
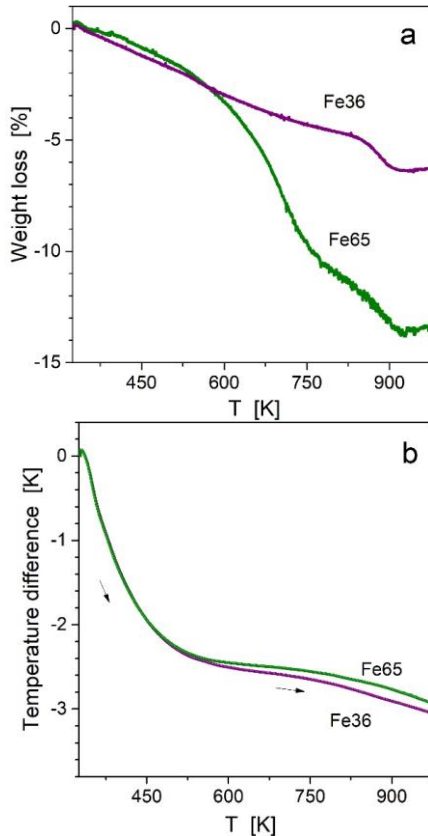
Figure 5. (a) TGA and (b) DTA curves corresponding to the first heating between room temperature and 950 K, at a rate of 10 K/min.

DTA measurements revealed a quite similar behavior in both arrays, with no sharp peaks observed during the first heating. Instead, small, and very wide maxima appear in the curves of both samples, starting near 520 K and reaching the maximum at about 750 K, indicating that a structural change takes place during the first heating. Then, it is concluded that during the first heating a given volume of the A1 γ- Fe$_x$Pd$_{100-x}$ solid solution transforms into an ordered phase (Fe$_3$Pd or FePd$_3$, depending on iron content) and the microstructure remains unchanged during subsequent

thermal cycles. As indicated above, the slope change in these subsequent cycles (**Figure 4**) observed near 500 K, corresponds to the Curie temperatures of the ordered stoichiometric phases Fe$_3$Pd and FePd$_3$.

Considering the data in Table 2, the microstructural scenario after thermal cycling consists of a majority ordered phase (Fe$_3$Pd or FePd$_3$, depending on iron content), in which grains of the remaining A1 γ- Fe$_x$Pd$_{100-x}$ minority phase are immersed. Then, to understand the magnetic properties of the samples below ~550 K, two ferromagnetic phases with different properties should be considered, while above this temperature the still ferromagnetic grains of the minority A1 γ- Fe$_x$Pd$_{100-x}$ phase (T$_C \sim 900$ K) become embedded in a paramagnetic matrix.

3.4 *Magnetic hysteresis*

Considering that no further changes in the magnetic polarization, $J(T)$, are observed after the first heating-cooling cycle, hysteresis loops of the biphasic NW arrays were subsequently measured at increasing temperature from 400 K to 900 K, under maximum applied field of $\pm$ 7 T. Two orthogonal field orientations relative to the NW axis were selected: PA configuration corresponds to the external magnetic field applied parallel to the NW axis and PE corresponds to the direction perpendicular to the NWs axis. Hysteresis curves measured at selected temperatures are shown in **Figure 6** and **Figure 7** for Fe36 and Fe65, respectively, displaying a restricted field interval of $\pm$ 0.2T ($\pm$ 0.03T in the inset) to illustrate the low field behavior.

It is found that both arrays are relatively soft ferromagnetic, exhibiting low coercivity. When loops measured in the PA and PE field configurations are compared an effective anisotropy is concluded with magnetization easy axis parallel to the NWs axis. Magnetostatic interaction among nanowires in the arrays can be also deduced from their reduced remanence. In fact, a small initial susceptibility arising from intense magnetostatic interactions is often observed in NW arrays; this low susceptibility rotates the hysteresis loop leading to the observed low remanence.
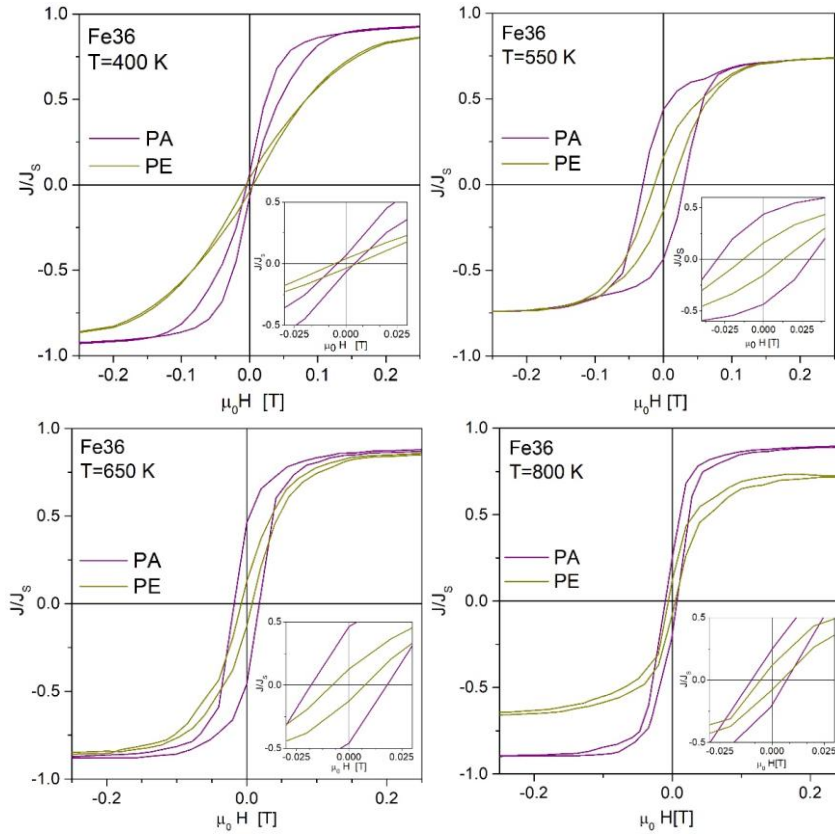
Figure 6. Hysteresis loops in PA and PE configurations at selected temperatures, corresponding to Fe36 measured after a first thermal cycle as described in **Figure 4a**.
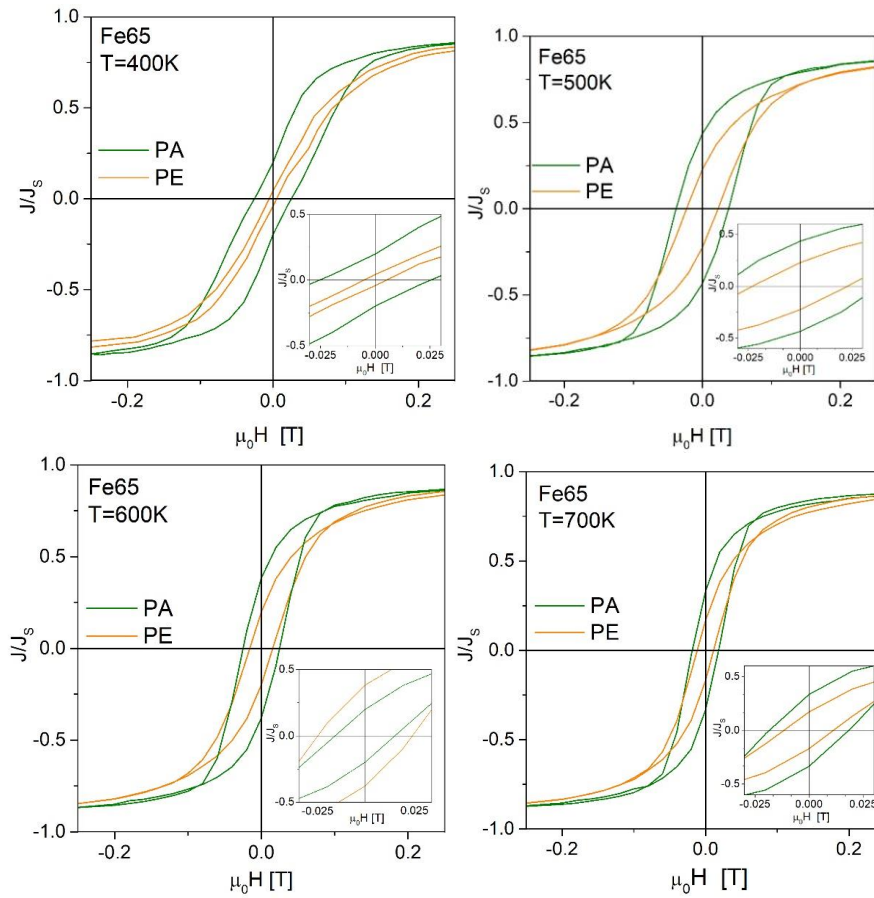

Figure 7. Hysteresis loops in PA and PE configurations at selected temperatures, corresponding to Fe65, measured *after* a first thermal cycle as described in **Figure 4b**.

3.5 *Temperature dependence of magnetic hysteresis properties*

The variation with temperature of the coercive field $\mu_0 H_C$ and the relative remanence or squareness ratio $S = J_R/J_S$ (with J_R and J_S the remanent and saturation polarization, respectively) in the biphasic arrays are depicted in **Figure 8**, in PA configuration.
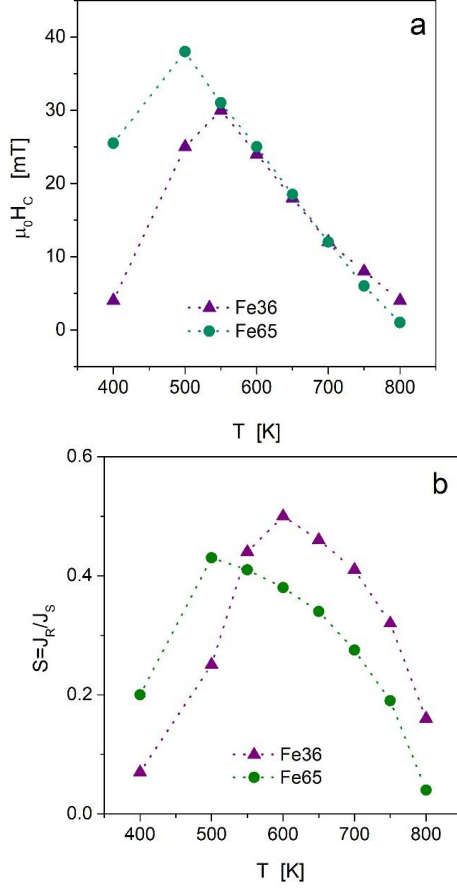

Figure 8. Coercive field, $\mu_0 H_c$, (a), squareness ratio, S, (b) as functions of temperature for samples Fe36 and Fe65. The size of the dots in the figure is proportional to the experimental error (estimated in 2%).

Both arrays are relatively soft, with coercivities below 40 mT, while the squareness S is always lower than 0.5. In both samples, the coercivity and squareness ratio exhibit a maximum near 550 K in Fe36 and 500 K in Fe65, at the Curie temperature of the ordered FePd$_3$ and Fe$_3$Pd phases in each array.

The temperature dependence of the effective uniaxial anisotropy constant K_{eff} of the biphasic NW arrays, consisting of a mixture of stable and metastable phases, was estimated from the hysteresis loops measured at different temperatures (some of them displayed in **Figure 6** and **Figure 7**), by applying the area method [33]. This method is based on the amount of energy stored in the NWs when they are magnetized to saturation in a given direction. Then, the effective anisotropy K_{eff} of each array is related to the area enclosed by the upper branches of the PA and PE magnetization curves. The temperature dependence of K_{eff} for each array is depicted in **Figure 9**.

Different contributions must be considered to estimate the effective anisotropy constant K_{eff}: i) the magnetocrystalline anisotropy K_C, ii) the magnetostatic shape anisotropy K_S and iii) the magnetostatic anisotropy K_I, associated to inter-wire magnetostatic interaction in the array. Then,

$$K_{eff} = K_C + K_S + K_I. \qquad (1)$$

An expression describing the magnetostatic contributions to the effective anisotropy constant (the one arising from intra-wire demagnetizing effects and the one arising from dipolar inter-wire interactions) is given in ref. [37]. Considering in addition a non-negligible contribution of the magnetocrystalline anisotropy, the effective constant can be written as:

$$K_{eff} = K_C + \frac{\mu_0 M_S^2}{4}(1 - 3P). \qquad (2)$$

Parameter P in Eq. 2 is the template's porosity, defined as $P = \pi/2\sqrt{3}(D/d_{cc})^2$ [38], which, in our case is 0.26 and is given by the template's characteristics.

The curves K_{eff} vs. T are shown in **Figure 9a** for Fe36 and in **Figure 9b** for Fe65. The contribution corresponding to the magnetostatic anisotropy K_{eff_calc}, calculated using the second term of Eq. (2), is also plotted for comparison.
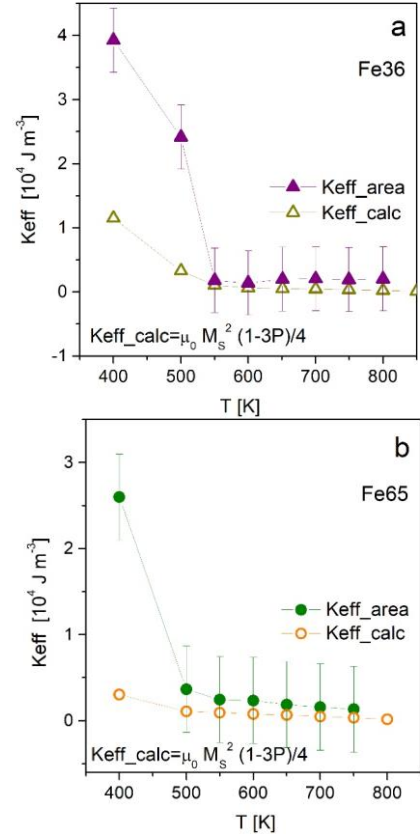

Figure 9. Effective magnetic anisotropy as a function of temperature for samples Fe36 (a) and Fe65 (b), estimated with the method of the hysteresis loop areas. The corresponding contribution from the shape anisotropy and magnetostatic interactions is also plotted in both pictures for comparison.

Above 550 K, the total effective anisotropy mostly arises from magnetostatic effects, such as shape and dipolar interactions anisotropies. On the contrary, below this temperature the contribution associated with the magnetocrystalline anisotropy K_C of the stoichiometric ordered phase in each sample should be considered, which vanishes above the Curie temperature. The difference of about 2-3 x 10^4 J m^{-3} observed near 400 K is consistent with values reported for $Fe_{68}Pd_{32}$ by Matsui et al. [39] for the magnetocrystalline constant of this phase near this temperature.

The microstructural scenario above 550 K consists of a mix of dispersed ferromagnetic γ−Fe(Pd) *fcc* grains in a larger volume of paramagnetic grains of the atomically ordered phases.

3.6 Magnetization reversal mechanism

The temperature dependence of the coercive field provides information about the magnetization reversal mechanism operating in the magnet. As shown in **Figure 8a** and **Figure 9**, a linear dependence may be considered at high temperatures.

The activation barrier *E* for magnetization reversal may be described by the general expression [40]:

$$E = E_0 \left[1 - \frac{H}{H_0}\right]^n \qquad (3)$$

where E_0 is the barrier height at zero applied field, H_0 is the external field at which the barrier vanishes, and *n* is an exponent which changes for the different mechanisms. For a mechanism of nucleation and further propagation of the domain wall it is *n* = 1, leading to a linear relationship, as that observed in **Figure 8a** above 550 K. Assuming that the thermal contribution to overcome the barrier is about 25 k_BT and that *n* = 1, the temperature dependence of the coercive field becomes:

$$\mu_0 H_C = \mu_0 H_0 - \alpha T, \qquad (4)$$

with $\alpha = \frac{25\, \mu_0 H_0\, k_B}{E0}$, leading to a barrier height $E_0 = \frac{25\, \mu_0 H_0\, k_B}{\alpha}$. From the fitting of Eq. (4) to the experimental data shown in **Figure 8a,** μ_0H_0 and E_0 may be estimated.

The coercive field *vs.* temperature curves in the TT condition are shown in **Figure 10a** and **Figure 10b**, for samples Fe36 and Fe65, respectively. Assuming that the effective anisotropy remains constant in the temperature range between 500 K and 800 K (see **Figure 9**), where the only ferromagnetic phase is the metastable A1 γ-Fe_xPd_{100-x} minority phase, quite good linear fits are obtained for each sample. The fitting parameters are listed in Table 3.
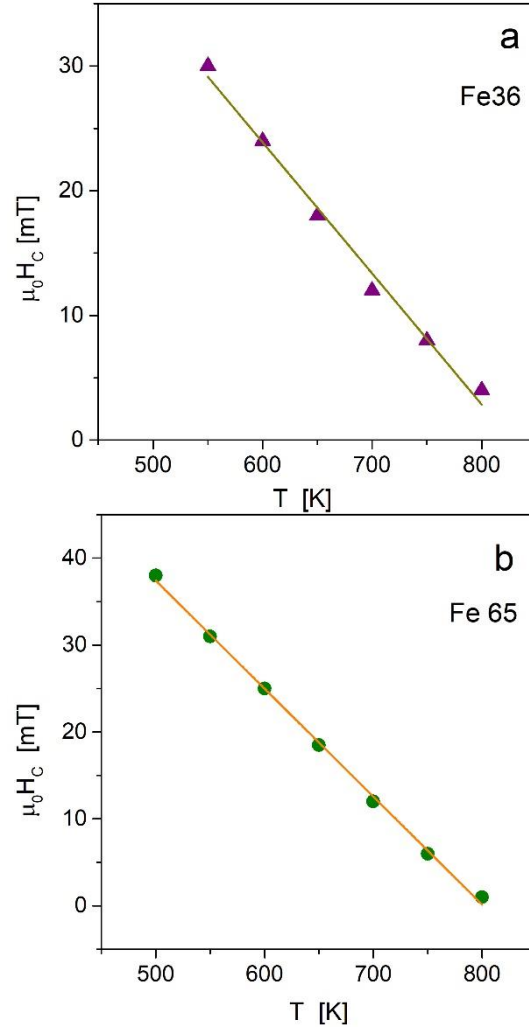
Figure 10. Coercive field measured in the PA configuration as a function of temperature, corresponding to samples (a) Fe36 and (b) Fe65. The size of the dots in the figure is proportional to the experimental error (estimated in 3%).

Table 3. Fitting parameters from the linear fits shown in **Figure 10**. The applied magnetic field under which the activation barrier vanishes $\mu_0 H_0$, the curve slope α and E_0, the apparent activation energy barrier at zero applied field, are listed.

	Fe 36	Fe65
$\mu_0 H_0$ [mT]	87±3	99±1
α [mT K^{-1}]	0.10 ± 0.01	0.12 ± 0.01
E_0 [eV]	1.7 ± 0.2	1.7 ± 0.2

The obtained activation energy values are comparable to those reported for a mechanism of nucleation of an inverse domain followed by expansion of domain walls in Fe (2 − 5 eV) and Ni (1.5 − 4 eV) [41] in relatively thin (12 − 50 nm) NWs, at low temperature. From the temperature dependence of the coercive field and the magnetic viscosity these authors conclude that magnetization reversal takes place via nucleation of small magnetic domains, located most likely at the end of the wires, followed by the movement of the domain wall. For biphasic Fe-Rh NWs 20 nm in diameter [7]

the low temperature values reported (2.3 - 3.1 eV) are also somewhat higher but comparable to those found in the present work.

The apparent activation energy is expected to depend on temperature through the effective anisotropy constant, which in turn depends on the saturation polarization and the magnetocrystalline anisotropy of the ferromagnetic phases in each sample. Then, different values may be expected at high temperature. From the data in **Figure 9** and the values of the parameters shown in Table 3, it is concluded that above the Curie temperatures of the ordered stoichiometric phases ($\sim$ 500 -550 K) hysteresis properties are practically independent of the NWs composition, which is consistent with the presence of only one ferromagnetic phase in the arrays, which is the A1-γ-Pd(Fe) solid solution.

4. Conclusion

The main phase in $Fe_{36}Pd_{64}$ and $Fe_{65}Pd_{35}$ nanowires, electrodeposited at 40 °C, is the metastable A1 γ-Pd(Fe) *fcc* disordered solid solution. This metastable phase is found to be ferromagnetic at room temperature, with a Curie temperature near 900 K.

During a thermal cycling between 300 K and 950 K, a volume fraction of this solid solution transforms into a stoichiometric ordered phase, being this phase $FePd_3$ for Fe36 and Fe_3Pd for the array with a higher iron content (Fe65). Despite the fact that the remaining A1 γ-Pd(Fe) is still metastable, this phase separation remains constant during subsequent thermal cycles up to 950 K.

The Curie temperatures of Fe_3Pd and $FePd_3$ are found to be about 500 K and 550 K, respectively. Above this temperature range, the biphasic NWs behave as a single ferromagnetic phase when the ordered phases become paramagnetic, and the hysteresis properties become those of the minority A1 γ-Pd(Fe) disordered metastable phase.

The temperature dependence of the coercive field in the arrays after thermal cycling, above about 550 K, is consistent with a mechanism involving the nucleation of inverse domains and the further expansion of the domain walls in the grains/grain clusters of the ferromagnetic phase, surrounded by the paramagnetic, majority ordered phase. The activation energy obtained is the corresponding to the metastable A1 γ-Pd(Fe) phase.

CRediT authorship contribution statement

Paula G. Bercoff: Conceptualization, Methodology, Validation, Formal analysis, Resources, Supervision, Validation, Visualization, Project administration, Funding acquisition, Writing – original draft, review & editing.
Eva Céspedes: Methodology, Validation, Investigation, Formal analysis, Writing – review & editing.
Soledad Aprea: Formal analysis, Investigation.
Silvia E. Urreta: Conceptualization, Methodology, Formal analysis, Visualization, Writing – original draft, review & editing.
José Luis Martínez: Validation, Investigation, Supervision, Resources, Writing – review & editing, Funding acquisition.
Manuel Vázquez: Resources, Writing – review & editing, Funding acquisition.

Data availability

The data that support the findings of this paper are available from the corresponding author upon reasonable request.

References

[1] R.W. Sibin Duan, Bimetallic nanostructures with magnetic and noble metals and their physicochemical applications, Progress in Natural Science: Materials International 23 (2013) 113–126. https://doi.org/10.1016/j.pnsc.2013.02.001

[2] Y.H. Huang, H. Okumura, G.C. Hadjipanayis, D. Weller, CoPt and FePt nanowires by electrodeposition, J. Appl. Phys. 91 (2002) 6869–6871. https://doi.org/10.1063/1.1447524

[3] M.S. Viqueira, N. Bajales, S.E. Urreta and P.G. Bercoff, Magnetization mechanisms in ordered arrays of polycrystalline $Fe_{100-x}Co_x$ nanowires, J. Appl. Phys. 117 (2015) 204302-9. https://doi.org/10.1063/1.4921701

[4] J. Alonso, H. Khurshid, V. Sankar, Z. Nemati, M.H. Phan, E. Garayo, J.A. García, H. Srikanth, FeCo nanowires with enhanced heating powers and controllable dimensions for magnetic hyperthermia, J. Appl. Phys. 117 (2015) 17D113. https://doi.org/10.1063/1.4908300

[5] S. Viqueira, G. Pozo-López, S.E. Urreta, A.M. Condó, D.R. Cornejo, and L.M. Fabietti, Cooperative nucleation modes in polycrystalline Co_xPd_{1-x} nanowires, J. Appl. Phys. 117 (2015) 204301-9. http://dx.doi.org/10.1063/1.4921700

[6] S. Viqueira, G. Pozo-López, S. E. Urreta, A. M. Condó, D. R. Cornejo and L. M. Fabietti, Magnetic hysteresis in ordered arrays of small-grained CoxPd1-x

nanowires, J. of Magn. Magn. Mater. 94 (2015) 185–194. https://doi.org/10.1016/j.jmmm.2015.06.033

[7] J.S. Riva, G. Pozo-López, A.M. Condó, L.M. Fabietti, S.E. Urreta. Low temperature ferromagnetism in Rh-rich Fe-Rh granular nanowires, Journal of Alloys and Compounds 747 (2018) 1008-1017. https://doi.org/10.1016/j.jallcom.2018.03.091

[8] M.S. Viqueira, S.E. García, S.E. Urreta, G. Pozo-López, L.M. Fabietti, Hysteresis properties of hexagonal arrays of FePd nanowires, IEEE Trans. on Magnetism 49 (8) (2013) 4498-4501.
http://dx.doi.org/10.1109/TMAG.2013.2258461

[9] M.S. Aprea, J.S. Riva, P.G. Bercoff, M. Vázquez, Temperature dependence of magnetic anisotropy in a cylindrical $Fe_{65}Pd_{35}$ nanowire array, J. of Magn. Magn. Mater. 564 (2022) 170166. https://doi.org/10.1016/j.jmmm.2022.170166

[10] E.G. Herrera, J.S. Riva, S. Aprea, O. Fernando Silva, P.G. Bercoff, A.M. Granados, FePd nanowires modified with cyclodextrin as improved catalysts: effect of the alloy composition on colloidal stability and catalytic capacity, Catalysis Science & Technology 12 (9) (2022) 2962-2971. https://doi.org/10.1039/D1CY02219A

[11] J.S. Riva, A.V. Juárez, S.E. Urreta, L.M. Yudi, Catalytic properties of FePd ferromagnetic nanowires at liquid/liquid interfaces, Electrochimica Acta 298 (2019) 379-388.
https://doi.org/10.1016/j.electacta.2018.12.069

[12] K. Fukamichi, Positive large linear magnetostriction in Fe-Pd crystalline alloys, J. Appl. Phys. 50 (1979) 6562-6563. https://doi.org/10.1063/1.325718

[13] M. Matsui K. Adachi, Magneto-elastic properties and invar anomaly of Fe-Pd alloys, Physica B 161 (1989) 53-59. https://doi.org/10.1016/0921-4526(89)90102-6

[14] A. Nan, R. Turcu, C. Tudoran, M. Sofronie, and A. Chiriac, Analysis of Functionalized Ferromagnetic Memory Alloys from the Perspective of Developing a Medical Vascular Implant, Polymers 14(7) (2022) 1397. DOI: 10.3390/polym14071397.

[15] F. Xiao, A. Bucsek, X. Jin, M. Porta, A. Planes, Giant elastic response and ultra-stable elastocaloric effect in tweed textured Fe-Pd single crystals, Acta Materialia 223 (2022) 117486. DOI: 10.1016/j.actamat.2021.117486.

[16] M. Cialone, F. Celegato, F. Scaglione, G. Barrera, D. Raj, M. Coïsson, P. Tiberto, P. Rizzi, Nanoporous FePd alloy as multifunctional ferromagnetic SERS-active substrate, Applied Surface Science 543 (2021) 148759. DOI: 10.1016/j.apsusc.2020.148759.

[17] J. Cui, R.D. James, Study of Fe_3Pd and related alloys for ferromagnetic shape memory, IEEE Transactions on Magnetics 37(4) (2001) 2675–2677. https://doi.org/10.1109/20.951271

[18] E.F. Wassermann, New Developments on the Invar-Effect, Physica Scripta T25 (1989) 209-219. https://doi.org/10.1088/0031-8949/1989/T25/038

[19] E.F. Wassermann. The Invar problem, J. Magn. Magn. Mater. 100 (1-2) (1991) 346-362. https://doi.org/10.1016/0304-8853(91)90828-X

[20] J. Koeda, Y. Nakamura, T. Fukada, T. Kakeshita, T. Takeuchi, K. Kishio, Giant magnetostriction in Fe-Pd alloy single crystal exhibiting martensitic transformation, Trans. Mat. Res. Soc. Jpn. 26 (2001) 215-218.

[21] Y.O. Kvashnin, S. Khmelevskyi, J. Kudrnovský, A.N. Yaresko, L. Genovese, P. Bruno. Noncollinear magnetic ordering in compressed $FePd_3$ ordered alloy: A first principles study, Phys. Rev. B 86 (2012) 174429-8. https://doi.org/10.1103/PhysRevB.86.174429

[22] M.L. Winterrose, M.S. Lucas, A.F. Yue, I. Halevy, L. Mauger, J.A. Muñoz, Jingzhu Hu, M. Lerche, B. Fultz, Pressure-Induced Invar Behavior in Pd_3Fe, Phys. Rev. Lett. 102 (2009) 237202-4. https://doi.org/10.1103/PhysRevLett.102.237202

[23] C.J. Ridley, C.L. Bull, NP. Funnell, S.C. Capelli. P. Manuel, D.D. Khalyavin, C.D. O'Neill, K.V. Kamenev, High-pressure neutron diffraction study of Pd_3 Fe, J. Appl. Phys. 125 (2019) 015901- 9. https://doi.org/10.1063/1.5079804

[24] Z. Cui, L. Li, A. Manthiram, J.B. Goodenough, Enhanced cycling stability of hybrid Li–air batteries enabled by ordered Pd_3Fe intermetallic electrocatalyst. J. Am. Chem. Soc. 137 (2015) 7278–7281. https://doi.org/10.1021/jacs.5b03865

[25] Z. Liu, G. Fu, J. Li, Z. Liu, L. Xu, D. Sun, Y. Tang, Facile synthesis based on novel carbon-supported cyanogel of structurally ordered Pd_3Fe/C as electrocatalyst for formic acid oxidation. Nano Res. 11(2018) 4686–4696. https://doi.org/10.1007/s12274-018-2051-7

[26] X. Weng, H. Ma, G. Owens, Z. Chen. Enhanced removal of 2,4-dichlorophenol by Fe-Pd@ZIF-8 via adsorption and dechlorination. Separation and Purification Technology 305 (2023) 122371. DOI: 10.1016/j.seppur.2022.122371.

[27] Y. Liu, G. Wang, W. Ma, N. Feng, J. Tong, X. Kang, T. Hu, H. Wu, Q. Yang, J. Xie. Preparation of magnetically separable and low-cost MC-FePd3 NPs with enhanced catalytic activity in the reduction of p-nitrophenol. Nanotechnology 34 (2023) 465701. DOI: 10.1088/1361-6528/aceafd.

[28] J. Liu, C. Peng, X. Shi. Preparation, characterization, and applications of Fe-based catalysts in advanced oxidation processes for organics removal: A review. Environmental Pollution 293 (2022) 118565. DOI: 10.1016/j.envpol.2021.118565.

[29] N. T. T. Nguyen , L. M. Nguyen, T. T. T. Nguyen, R. K. Liew, D. T. C. Nguyen, T. V. Tran. Recent advances on botanical biosynthesis of nanoparticles for catalytic, water treatment and agricultural applications: A review. Science of The

Total Environment 827 (2022) 154160. DOI: 10.1016/j.scitotenv.2022.154160.

[30] B. Massalsky, Binary Alloys Phase Diagrams, ASM International Materials Park, Ohio, 1986.

[31] H. Yabe, R.C. O'Handley, T. Kuji. J. Magn. Magn. Mater. 310 (2007) 2500-2502. https://doi.org/10.1016/j.jmmm.2006.11.094

[32] T. B. Massalsky, Binary Alloys Phase Diagrams, ASM International Materials Park, Ohio, 1986.

[33] P. Mohn, E. Supanetz, K. Schwarz, Electronic structure and spin fluctuations in the fcc Fe-Pd system, Australian Journal of Physics 46 (1993) 651-663. https://doi.org/10.1071/PH930651

[34] E. Burzo, P. Vlaic. Magnetic properties of iron-palladium solid solutions and Compounds, Journal of Optoelectronics and Advanced Materials 12 (9) (2010) 1869–1878.

[35] C.J. Ridley, C.L. Bull, N.P. Funnell, S.C. Capelli, P. Manuel, D.D. Khalyavin, C.D. O'Neill, K.V. Kamenev, High-pressure neutron diffraction study of Pd_3Fe, J. Appl. Phys. 125, 015901 (2019). https://doi.org/10.1063/1.5079804

[36] J. Cui, Study of Fe_3Pd and related alloys for ferromagnetic shape memory, IEEE Transactions on Magnetics 37(4) (2001) 2675–2677. https://doi.org/10.1109/20.951271

[37] P. Carignan, C. Lacroix, and A. Ouimet, M. Ciureanu, A. Yelon, D. Ménard, Magnetic anisotropy in arrays of Ni, CoFeB, and Ni/Cu nanowire, J. Appl. Phys. 102 (2) (2007) 023905-10. https://doi.org/10.1063/1.2756522

[38] K. Nielsch, F. Müller, A-P. Li, U. Gösele. Uniform nickel deposition into ordered alumina pores by pulsed electrodeposition, Advanced Materials 12 8 (2000) 582-586. https://doi.org/10.1002/(SICI)1521-4095(200004)12:8<582::AID-ADMA582>3.0.CO;2-3

[39] M. Matsui, J.P. Kuang, T. Totani and K. Adachi, Magnetic anisotropy of Fe-Pd invar alloys, J. of Magn. Magn. Mater. 54-57 (1986) 911-912. https://doi.org/10.1016/0304-8853(86)90310-0

[40] P. Gaunt, Magnetic viscosity and thermal activation energy, J. Appl. Phys. 59 (1986) 4129-4132. https://doi.org/10.1063/1.336671

[41] P.M. Paulus, F. Luis, M. Kröll, G. Schmid and L.J. de Jongh, Low-temperature study of the magnetization reversal and magnetic anisotropy of Fe, Ni, and Co nanowires J. of Magn. Magn. Mater. 224 (2001) 180-196. https://doi.org/10.1016/S0304-8853(00)00711-3

✝✝✝✝✝